



Article

Comparison of Cloud Properties from Himawari-8 and FengYun-4A Geostationary Satellite Radiometers with MODIS Cloud Retrievals

Ruize Lai ^{1,2}, Shiwen Teng ¹, Bingqi Yi ^{3,4} , Husi Letu ⁵ , Min Min ^{3,6} , Shihao Tang ⁶ and Chao Liu ^{1,2,*}

¹ Collaborative Innovation Center on Forecast and Evaluation of Meteorological Disasters, Nanjing University of Information Science & Technology, Nanjing 210044, China

² Key Laboratory for Aerosol-Cloud-Precipitation of China Meteorological Administration, School of Atmospheric Physics, Nanjing University of Information Science & Technology, Nanjing 210044, China

³ School of Atmospheric Sciences and Guangdong Province Key Laboratory for Climate Change and Natural Disaster Studies, Sun Yat-sen University, Guangzhou 510275, China

⁴ Southern Marine Science and Engineering Guangdong Laboratory (Zhuhai), Zhuhai 51900, China

⁵ State Key Laboratory of the Science and Remote Sensing, Institute of Remote Sensing and Digital Earth, Chinese Academy of Sciences, Beijing 100101, China

⁶ Key Laboratory of Radiometric Calibration and Validation for Environmental Satellites, National Satellite Meteorological Center, China Meteorological Administration, Beijing 100081, China

* Correspondence: chao_liu@nuist.edu.cn; Tel.: +86-158-5189-1106

Received: 31 May 2019; Accepted: 17 July 2019; Published: 18 July 2019



Abstract: With the development and the improvement of meteorological satellites, different instruments have significantly enhanced the ability to observe clouds over large spatial regions. Recent geostationary satellite radiometers, e.g., Advanced Himawari Imager (AHI) and Advanced Geosynchronous Radiation Imager (AGRI) onboard the Himawari-8 and the Fengyun-4A satellite, respectively, provide observations over similar regions at higher spatial and temporal resolutions for cloud and atmosphere studies. To better understand the reliability of AHI and AGRI retrieval products, we compare their cloud products with collocated Moderate Resolution Imaging Spectroradiometer (MODIS) cloud products, especially in terms of the cloud optical thickness (COT) and cloud effective radius (CER). Our comparison indicates that cloud mask and cloud phase of these instruments are reasonably consistent, while clear differences are noticed for COT and CER results. The average relative differences (RDs) between AHI and AGRI ice COT and that of MODIS are both over 40%, and the RDs of ice CER are less than 20%. The consistency between AHI and MODIS water cloud results is much better, with the RDs of COT and CER being 29% and 9%, respectively, whereas the RDs of AGRI COT and CER are still larger than 30%. Many factors such as observation geometry, cloud horizontal homogeneity, and retrieval system (e.g., retrieval algorithm, forward model, and assumptions) may contribute to these differences. The RDs of COTs from different instruments for homogeneous clouds are about one-third smaller than the corresponding RDs for inhomogeneous clouds. By applying unified retrieval systems based on the forward radiative transfer models designed for each particular band, we find that 30% to 70% of the differences among the results from different instruments are caused by the retrieval system (e.g., different treatments or assumptions for the retrievals), and the rest may be due to sub-pixel inhomogeneity, parallax errors, and calibration.

Keywords: AHI; AGRI; MODIS; cloud products

1. Introduction

Clouds, covering approximately 65%–70% of the globe on average, are one of the most important components of the Earth's atmosphere [1]. Clouds have a crucial impact on the Earth's radiation budget by affecting the incoming solar and outgoing thermal radiation [2,3]. Due to their complex microphysical properties, e.g., vertical and horizontal inhomogeneity, diversity in particle phase and shape, and temporal variations, there are still significant uncertainties in our understanding of cloud properties [4–6]. Accurately describing cloud optical and microphysical properties has always been a popular research topic.

To better understand the characteristics of clouds, a large number of observations have been carried out using different observational methods at various scales, e.g., cloud chamber observations [7], in situ and airplane measurements [8], cloud radars [9], and satellite remote sensing [10]. Among these methods, satellites can provide continuous observations over large-scale spatial regions and long-term durations, and they have become one of the essential tools for understanding cloud properties [11]. The satellite radiometer is a fundamental and popular onboard instrument for cloud studies. For example, polar-orbiting radiometers (e.g., Moderate Resolution Imaging Spectroradiometer, MODIS, onboard the Aqua and the Terra satellites) have widely been used to illustrate the global distributions of cloud fraction, cloud mask, cloud optical thickness (COT), top height (CTH), and temperature (CTT) for both ice and liquid water clouds [12–15]. Active sensors, such as millimeter wavelength cloud profiling radar (CPR) [16] and cloud-aerosol lidar with orthogonal polarization (CALIOP) [17] onboard CloudSat and CALIPSO, respectively, can provide the vertical distribution of clouds, but their observation spatial scale is relatively limited. In addition, the U.S. Geostationary Operational Environmental Satellites-R (GOES-R) series can nearly continuously observe the clouds of target areas based on their characteristics and develop their own cloud products [18].

The Japanese and the Chinese meteorological organizations recently launched new generation geostationary meteorological satellites, i.e., the Himawari-8 (H-8) and the FengYun-4A (FY-4A), on 7 October 2014, located at 140.7 °E, and 11 December 2016, located at 104.7 °E, respectively [19,20]. H-8 and FY-4A provide similar temporal, spatial, and spectral resolution measurements with advanced imagers. There are notable differences between H-8 and FY-4A radiometers. The H-8 spacecraft carries an Advanced Himawari Imager (AHI) with 16 bands from 0.47 μm to 13.3 μm [three visible (VIS), three near-infrared (NIR), and 10 infrared (IR)], and AHI can take measurements every 10 min for a full disk and every 2.5 min for Japan and other certain target areas. The satellite spatial resolutions of AHI range from 0.5 km to 2 km at sub-satellite point [21,22]. FY-4A is equipped with an Advanced Geosynchronous Radiation Imager (AGRI), a Geostationary Interferometric InfraRed Sounder, and a Lightning Mapping Imager. The AGRI has 14 spectral bands from 0.45 μm to 13.8 μm (two VIS, six NIR, and six IR). The temporal resolution of AGRI is 15 min for a full disk, and the highest spatial resolution is 0.5 km at sub-satellite point in the 0.65 μm band [23].

Both AHI and AGRI offer various physical products for clouds, aerosols, sea surfaces, wildfires, photosynthetically active radiation, and so on [20,21]. Compared with polar-orbiting satellite radiometers, geostationary satellite radiometers can observe a target area at a high temporal resolution to provide temporally continuous cloud product data. Because of their high temporal resolution and large spatial coverage, those radiometers can continuously observe atmosphere in Asia and infer detailed cloud information, including cloud mask, types, microphysical and optical properties, and cloud life cycles. These products are widely used for weather analysis and forecasting, short-term climate prediction, and environmental and disaster monitoring in Asia [19–21]. For example, Chen et al. [24] discussed the vertical distributions and the diurnal variations in the cloud top over East Asia using the AHI/H-8 cloud products. Shang et al. [25] evaluated the quality of AHI cloud mask and studied the diurnal and the seasonal variations in clouds over the Tibetan Plateau using the AHI/H-8 hourly cloud mask products.

However, our understanding of the quality of different satellite cloud products is still limited, and there are still significant uncertainties in cloud products themselves. Several factors may contribute to the differences between different cloud products. For example, the characteristics and the differences

between different versions of MODIS cloud products have been emphasized, e.g., between collection 4 (C4) and collection 5 (C5) [12,26,27] and between collection 5 and collection 6 (C6) [28]. Yi et al. [29–31] found that the differences between MODIS C5 and C6 cloud products are mainly caused by changes in ice particle model (ice particle shape and surface roughness). For products from different instruments, the differences are even more significant. Zhang et al. [32,33] indicated that the differences in COT between Polarization and Directionality of Earth's Reflectances (POLDER) and MODIS are mainly due to different ice particle models used in their retrieval algorithms. Instrument resolution, classification of cloud phase, and observation geometry all contribute to the uncertainties in cloud products from different satellites [34]. Kahn et al. [35] found that the differences between Atmospheric Infrared Sounder (AIRS) and MODIS ice cloud properties vary for pixels with different surface types, latitudes, cloud vertical distributions, etc. Moreover, the vertical heterogeneity of ice clouds has an important effect on cloud property retrieval of passive remote sensing [36,37]. Thus, to better describe the cloud properties and to understand climatology using satellite observations, the quality of cloud products themselves should be known. The cloud products of AHI and AGRI were briefly discussed during product development [22,38]. Due to the short time since release, there is still a lack of in-depth comparisons of AHI and AGRI products. Furthermore, most of those studies reveal only the differences between different products and do not sufficiently discuss the reasons underlying these differences.

As a result, this study discusses not only the differences between AHI (AGRI) and MODIS cloud products but also the potential factors causing these differences. The details of MODIS, AHI, and AGRI instruments and their cloud products as well as the collocation methods are introduced in Section 2, and Section 3 compares the cloud products of the three instruments. The factors to which the differences in the three products may be attributed, especially their retrieval system, are discussed in Section 4, and Section 5 concludes this study.

2. Data and Methods

This study evaluates the cloud characteristics retrieved from two geostationary satellites through comparison with the operational cloud products from MODIS [28]. MODIS is one of the most successful sensors onboard the polar-orbiting satellites Aqua and Terra [39]. MODIS includes 36 spectral bands ranging from 0.4 to 14.2 μm and covering almost all key bands [12]. MODIS takes a granule image every 5 min. During twenty years of observations, the MODIS operational cloud retrieval algorithm has been continuously updated and enhanced, and its products have been well validated through comparison with active remote sensing data and radiance simulations [13,26,27,39–41]. The retrieval uncertainties of the latest version, i.e., MODIS C6 products, in terms of the COT and the cloud effective radius (CER) are reported to be less than 5% [28]. MODIS provides some of the most reliable cloud properties, revealing the distribution of global clouds and quantifying the cloud microphysical, optical, and radiative properties [12,26,42–44]. In this study, we consider only the cloud product data from Aqua to avoid differences between those of Aqua and Terra [12].

The level-2 cloud products of AHI, AGRI, and MODIS (i.e., H8_L2_CLP, FY4A_L2_Cloud, and MYD06_L2, respectively) are employed in this study, and cloud mask, cloud phase, COT, and CER are considered for comparison. To cover as many observational conditions as possible, we select observations at an overlapping region with the AHI and the AGRI observations (80°E–150°E, 60°N–60°N) from four seasons, i.e., July and October of 2017 and January and April of 2018. The results of five days from each month are considered, resulting in a total of over 150 collocated MODIS granules (approximately 5–10 MODIS granules per day). We find that the results are statistically stable (i.e., there is no significant difference upon considering more data), and therefore, we think that the current dataset is enough for our study.

Cloud mask is a fundamental product for satellite applications because the other cloud properties can be retrieved only for pixels that are determined to be cloudy pixels. MODIS, AHI, and AGRI use multispectral threshold algorithms based on different spectral characteristics of VIS, NIR, and IR bands under cloudy and clear conditions to obtain cloud mask information [45,46]. MODIS observations from

20 spectral bands are considered for threshold tests with different surface types to produce its cloud mask results [45]. Due to the band design, less information is applied by AHI and AGRI [20,21]. AHI uses nine bands for a sequence of cloud tests [46], such as top temperature, emissivity and reflectance tests, cloud and atmospheric absorption tests, etc. Observations from six AGRI bands are used to perform 13 spectral and spatial uniformity tests and 2 restore tests [47]. The cloud masks of AHI, AGRI, and MODIS all classify pixels into four levels, including clear, probably clear (pro-clear), probably cloudy (pro-cloudy), and cloudy. In this study, the cloud thermodynamic phase product of MODIS, i.e., Cloud_Phase_Optical_Properties in MYD06 product, is considered, and the cloud phase results are determined through a combination of shortwave infrared (SWIR) and IR tests. The algorithm uses new voting logic and a series of tests (including an IR phase test, CTT tests, a 1.38 μm test, and independent ice and liquid phase spectral CER tests) [48]. In the AHI cloud phase algorithm, the ratios of the reflectances of 0.6 and 1.6 μm bands and the brightness temperatures of 11.2 and 8.6 μm bands are used [49]. For AGRI, the classical cloud emissivity algorithm is used to identify cloud phase based on 7.3, 8.6, 11, and 12 μm bands [38,50].

The cloud optical property products of MODIS, AHI, and AGRI are based on the bi-spectral method introduced by Nakajima and King [51], which uses the reflectance of a cloud non-absorbing band (sensitive to COT) and a cloud absorbing band (sensitive to both COT and CER), but different parameter assumptions and forward models are employed and developed. The MODIS C6 algorithm employs a lookup table (LUT) of non-absorbing and absorbing bands to retrieve COT and CER. Three different pairs of non-absorbing and absorbing bands are used for land, ocean, and ice surfaces, respectively [28]. Various physical parameters of atmosphere and clouds, such as atmospheric temperature profile, moisture profile, and surface albedo, are also needed as auxiliary data in the retrieval process [52]. The Comprehensive Analysis Program for Cloud Optical Measurement (CAPCOM) algorithm developed by Nakajima and Nakajima [53] and Kawamoto et al. [54] is employed to retrieve the cloud properties of AHI [27], and Band 3 (0.64 μm) and Band 6 (2.3 μm) of AHI are used for all surface types. The ancillary dataset used in the CAPCOM algorithm can be quite different from that used in the MODIS C6 algorithm. The cloud products of AGRI are developed based on the science product algorithm testbeds of Fengyun Geostationary Algorithm Testbed-Imager/Sounder [38]. Similar to the AHI CAPCOM algorithm, the AGRI COT and the CER are obtained by using a Daytime Cloud Optical and Microphysical Property (DCOMP) algorithm based on the observed reflectances at 0.65 and 2.25 μm bands and a one-dimension variational (1DVAR) algorithm [38,55]. To conclude, the key bands used by MODIS, AHI, and AGRI to retrieve cloud mask, phase, and microphysical and optical properties are given in Table 1. Note that only the central wavelengths of corresponding bands are listed in the table, and the detailed spectral response functions of similar bands from different instruments could be significantly different, which contributes to the differences between different cloud results.

Table 1. Spectral bands used for cloud mask, phase, and microphysical and optical property retrieval of the Moderate Resolution Imaging Spectroradiometer (MODIS), the Advanced Himawari Imager (AHI), and the Advanced Geosynchronous Radiation Imager (AGRI).

	Cloud Mask and Phase (μm)	Microphysical and Optical Properties (μm)
MODIS	0.659, 0.865, 0.470, 0.555, 1.240, 1.640, 2.130, 0.415, 0.443, 0.905, 0.936, 3.750, 3.959, 1.375, 6.715, 7.325, 8.550, 11.030, 12.020, 13.335, 13.935	0.66, 0.86, 1.24, 1.6, 2.10, 3.7
AHI	0.64, 0.86, 1.6, 3.9, 7.3, 8.6, 10.4, 11.2, 12.4	0.64, 2.30
AGRI	0.65, 1.6, 3.8, 7.12, 8.6, 11.0, 12.09	0.65, 2.25

For cloud models in different retrieval algorithms, the differences in water clouds can be minor, as the same spherical particles and the Lorenz–Mie theory are normally applied [22,28], although

the size distribution and the water refractive index considered can still be different. However, quite different models are used for ice cloud representation. The ice crystal model based on severely roughened column aggregates is used in the MODIS C6 retrieval algorithm [28,56]. A model named Voronoi particles (i.e., irregularly shaped aggregates with a roughness related to the particle size) is used to present the scattering properties of ice particles in the CAPCOM algorithm [57]. The AGRI employs a mixture model with droxtals, hollow and solid columns, hexagonal plates, three-dimensional (3D) bullet rosettes, and aggregates developed by Baum et al. [58], i.e., the model used for the MODIS Collection 5 cloud product. For the treatment on surface, AHI employs its self-developed clear-sky surface reflectivity library as the surface albedo [22], and the surface albedo dataset of corresponding MODIS product is used for AGRI retrievals [55].

Due to different observation times and locations of MODIS, AHI, and AGRI, it is necessary to stringently collocate the cloud product data from the three instruments in time and space to perform a fair comparison. First, the cloud product data with a time difference of less than 5 min (MODIS observation time) among the three different satellites are selected in this study; we assume that the cloud properties do not change significantly during the 5 min time interval. In addition, the spatial resolutions of MODIS, AHI, and AGRI level-2 cloud products employed in this study are 1 km, 5 km, and 4 km, respectively. The level-2 cloud products of MODIS are collocated for those of the AHI and the AGRI pixels, which facilitates a point-to-point comparison. The collocation method used in this paper is similar to that of Li et al [59]. The low-resolution AHI and AGRI are considered to be primary sensors, and the high-resolution MODIS is considered to be an accessory sensor. If the distance between a MODIS pixel center and a primary sensor (AHI or AGRI) pixel center is less than half of the primary sensor resolution, we count the MODIS pixel as a collocated pixel. In other words, we look for all MODIS pixels within a primary sensor (AHI or AGRI) pixel circle that has a diameter of its spatial resolution. Thus, the collocated low-resolution MODIS COT can be obtained by a weighted average as:

$$\text{COT} = \frac{\sum_{i=1}^N \left[\left(1 - \frac{r_i^2}{R^2} \right) \text{COT}_i \right]}{\sum_{i=1}^N \left(1 - \frac{r_i^2}{R^2} \right)} \quad (1)$$

where r and R are the distance from the accessory sensor pixel to the primary sensor pixel and half of the resolution of the primary sensor, respectively. N is the number of accessory sensor pixels in the primary sensor pixel, as defined above. For CER, the COT of each pixel should also be considered during the weighted average; thus, the collocated CER is given by:

$$\text{CER} = \frac{\sum_{i=1}^N \left[\left(1 - \frac{r_i^2}{R^2} \right) \text{COT}_i \text{CER}_i \right]}{\sum_{i=1}^N \left[\left(1 - \frac{r_i^2}{R^2} \right) \text{COT}_i \right]} \quad (2)$$

After collocation, the original high-resolution (1 km) MODIS products are transformed into those with the spatial resolutions of AHI (5 km) and AGRI (4 km), respectively. The MODIS cloud optical property product reports COT/CER only for successful retrieval pixels; thus, only pixels that have a successful retrieval rate of over 95% are considered to be successfully collocated pixels.

In the collocation processes of cloud mask and phase, the types of all pixels of the accessory sensors that meet the collocation condition are counted. In the primary sensor pixel resolution, only if the number of a certain type accounts for more than 95% of whole pixels of accessory sensors is its type considered to be a collocated pixel type; otherwise, the collocated pixel type is considered invalid. With the 95% threshold, approximately 20% of pixels are excluded due to partially cloudy and partially clear conditions. The categories of AHI, AGRI, and MODIS cloud phases are different, and we consider only ice, liquid water, and mixed-phase clouds in the comparison.

It should be noted that the calibration accuracy directly affects quantitative retrievals and consequently the comparability among results from different instruments. However, it is difficult even

to understand absolute L1B reflectance errors of one instrument [60,61], and their further effects on the retrieved results are not considered in this study. In other words, we assume the differences caused by calibration errors are much less than the differences among cloud properties of different instruments.

3. Products Comparison

With the MODIS cloud properties collocated to those of the two geostationary radiometers, it is straightforward to compare the properties pixel by pixel. Table 2 presents the fractions of the pixels of MODIS, AHI, and AGRI cloud mask and phase. For cloud mask, the AGRI fractions are quite similar to the MODIS results with differences of less than 2%. The differences between AHI and MODIS for pro-cloudy and cloudy are greater than 10%. The number of pro-cloudy pixels may be overestimated by AHI, whereas the number of cloudy pixels classified by AHI is smaller than that of MODIS. For cloud phase, the results of the three instruments show good consistency, especially for liquid water cloud pixels, with differences less than 1%. AHI and AGRI have differences of ~6% for mixed and ice cloud pixels compared with those of MODIS.

Table 2. Comparisons of AHI and AGRI cloud mask and phase results. The values shown are the proportions of pixels classified as each category.

	Cloud Mask				Cloud Phase		
	clear	pro-clear	pro-cloudy	cloudy	Water	Mixed	Ice
MODIS	22%	4%	15%	59%	52%	1%	47%
AHI	22%	1%	29%	48%	52%	7%	41%
AGRI	23%	2%	14%	61%	53%	4%	43%

Figure 1 shows the proportions of cloud mask results in AHI and AGRI based on the MODIS cloud mask results. Differently colored rectangles of the histograms represent the portions of the particular AHI (AGRI) classifications for the MODIS pixels classified as each category (clear, pro-clear, pro-cloudy, and cloudy from left to right). The portion of AHI (AGRI) pixels from a particular type corresponding to the same MODIS classification can be understood as hit rate (HR) (can be interpreted as accuracy), and the difference between the HR and the unit is known as the false-alarm rate (FAR), i.e., $FAR = 1 - HR$. If we assume there are a total of A collected MODIS clear pixels, the AHI (AGRI) clear HR is the ratio of B to A, i.e., $RH = B/A$, where B is the number of pixels categorized as clear by AHI (AGRI) among all MODIS clear pixels (i.e., of A MODIS pixels), and the corresponding AHI (AGRI) clear FAR is the portion of the rest $(A - B)/A = 1 - HR$. In the figure, the proportion of red rectangles in the leftmost pair of the histograms, i.e., for MODIS clear pixels, is AHI (AGRI) clear HR, and the sum of the rest of the rectangles is AHI (AGRI) clear FAR. Overall, the clear and cloudy results of AHI and AGRI are in good agreement with those of MODIS with high confidence. Over 75% of the pixels classified as clear pixels by MODIS are also categorized as clear by AHI and AGRI. For cloudy pixels, the HR values of AHI and AGRI are 77% and 93%, respectively. It is worth noting that the classification results of AHI and AGRI for pro-clear and pro-cloudy pixels are significantly different from those of MODIS with the FARs all larger than approximately 70%. For AHI cloud mask, more than 65% and 20% of pro-clear pixels classified by MODIS are categorized as clear and pro-cloudy pixels, respectively. More than 50% and 25% of the pro-cloudy pixels categorized by MODIS are identified as clear and cloudy pixels in AGRI, respectively. The main reason for these differences is different theoretical methods used in these instruments for identifying pro-clear and pro-cloudy pixels. Meanwhile, we also count the HRs for all clear (clear + pro-clear) and cloudy (pro-cloudy + cloudy) pixels of these instruments, and the combined results show a little discrepancy. For all clear pixels, i.e., clear + pro-clear, AHI HR is 78%, and AGRI HR is 80%. For cloudy + pro-cloudy, the HRs of AHI and AGRI are both over 95%. This result indicates that both AHI and AGRI overclassify some MODIS clear pixels as cloudy ones.

Figure 2 is similar to Figure 1 but for cloud phase. AHI cloud phase shows HR values above 90% and 80% for liquid water and ice cloud pixels, respectively, and the HR drops to ~40% for the mixed-phase cloud pixels. AHI defines more than 40% of the mixed-phase cloud pixels classified by MODIS as liquid water cloud pixels. AGRI ice and liquid water cloud pixels are similar to that of MODIS with HR values of 83% and 91%, respectively. The most significant differences between AGRI and MODIS are for mixed-phase clouds that have a FAR of ~75%, because some of the mixed-phase cloud pixels classified by MODIS algorithm are understood to be either water or ice clouds by the AGRI algorithm.

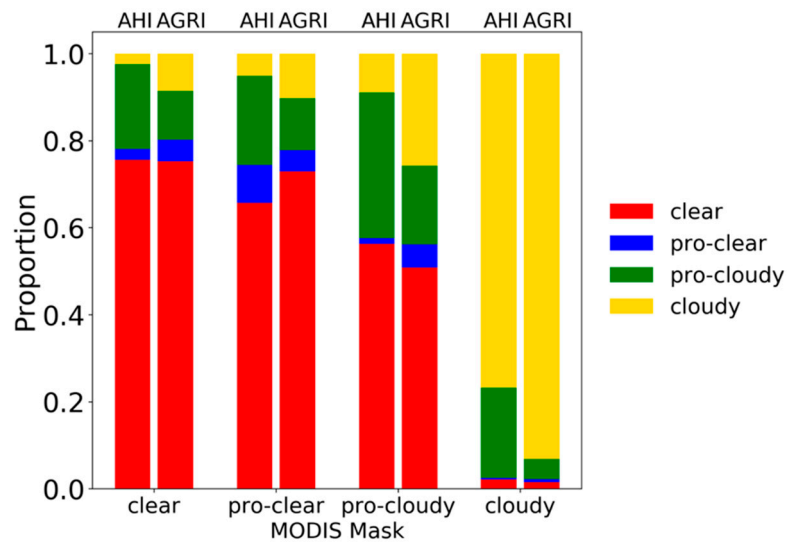


Figure 1. The proportions of clear, pro-clear, pro-cloudy, and cloudy pixels in AHI and AGRI for particular MODIS pixels. The left column of each pair of columns indicates the AHI result, and the right column is the AGRI result.

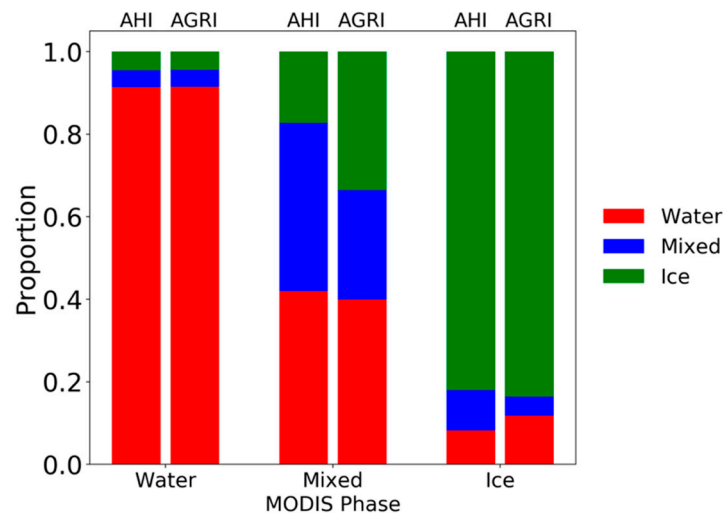


Figure 2. Same as Figure 1 but for cloud phase (i.e., water clouds, mixed-phase clouds, and ice clouds).

To quantitatively compare COT and CER, five parameters, i.e., the intraclass correlation coefficient (ICC), the average relative difference (RD), the slope (K) and the intercept (B) from the linear regression, and the standard deviation (Std), are used to quantify the relationships between two datasets from different satellites. The definition of ICC is:

$$ICC = \frac{\sum_{i=1}^N (x_{1i} - \bar{x})(x_{2i} - \bar{x})}{(N-1)s_x^2} \quad (3)$$

where N is the number of total collocated pixels. x_{1i} and x_{2i} are the measuring values of the two datasets, and \bar{x} and s_x^2 are the pooled mean and the corresponding standard deviation, respectively. Thus, ICC reflects the correlation between two datasets more intuitively. With a range between 0 and 1, larger ICC values indicate higher correlations between the two datasets. To avoid the canceling out of positive and negative RDs, the average RD is defined for the absolute values according to:

$$RD = \frac{1}{N} \sum_{i=1}^N \left| \frac{x_i - x_{oi}}{x_{oi}} \right| \quad (4)$$

where x_i and x_{oi} are the AHI (AGRI) and the MODIS results, respectively. K and B are used to represent the linear relationships between different results, and their rigorous definitions are not listed here. The Stds for the differences between the AHI (AGRI) and the MODIS results are considered here, and they are given by:

$$Std = \sqrt{\frac{\sum_{i=1}^N (\Delta x_i - \overline{\Delta x})^2}{N - 1}} \quad (5)$$

where Δx_i and $\overline{\Delta x}$ are the AHI (AGRI) and the MODIS difference and the corresponding average difference, respectively. Table 3 shows statistical results comparing the ice and the liquid water cloud properties from AHI (AGRI) and MODIS.

Figure 3 illustrates pixel-to-pixel comparison of ice COT and the CER between the AHI (AGRI) and the MODIS results. Note that only pixels that are classified as ice clouds by all three cloud phase products are considered here for comparison. The top and the bottom rows are for AHI and AGRI, respectively. The ICC between AHI and MODIS ice COTs is approximately 0.80, and the corresponding RD is ~40%. The AGRI ice COT is found to be notably larger than its MODIS counterpart, and its RD is even over 100%. Moreover, the AHI ice CER values are also larger than their MODIS counterparts, and the slope is 1.19. However, the AGRI ice CERs are underestimated overall compared to those of MODIS, and the disagreement is clearly shown by the statistical parameters, especially the slope of 0.37.

Table 3. Statistics of cloud optical thickness (COT) and cloud effective radius (CER) of the ice and the liquid water cloud comparison from AHI, AGRI, and MODIS, including the slope (K) and the intercept (B) of the linear regression equation, the intraclass correlation coefficient (ICC), the average relative difference (RD), and the standard deviation (Std).

		AHI					AGRI				
		K	B	ICC	RD	Std	K	B	ICC	RD	Std
Ice	COT	0.98	0.75	0.80	43.3%	1.8	1.34	1.66	0.46	114.1%	2.3
	CER	1.19	−1.85	0.33	16.1%	4.8	0.37	17.28	0.23	11.8%	3.6
Water	COT	0.96	0.78	0.88	29.4%	1.9	1.02	1.96	0.66	60.6%	2.3
	CER	0.83	1.29	0.89	8.6%	1.1	1.07	2.86	0.39	31.6%	2.1

Figure 4 shows the histogram distributions of ice COT and CER given by the three instruments. The overall distributions are similar, although some differences can be noticed. AGRI gives thicker ice clouds (those with COTs > 16) than those of MODIS due to the systematic overestimation. The CER distributions of MODIS and AGRI are relatively narrow, and that of AHI is wider. The MODIS and AGRI CERs both show peaks at approximately 30 μm , while another peak at approximately 12 μm is also observed for AGRI CER, which may be caused by a retrieval artifact.

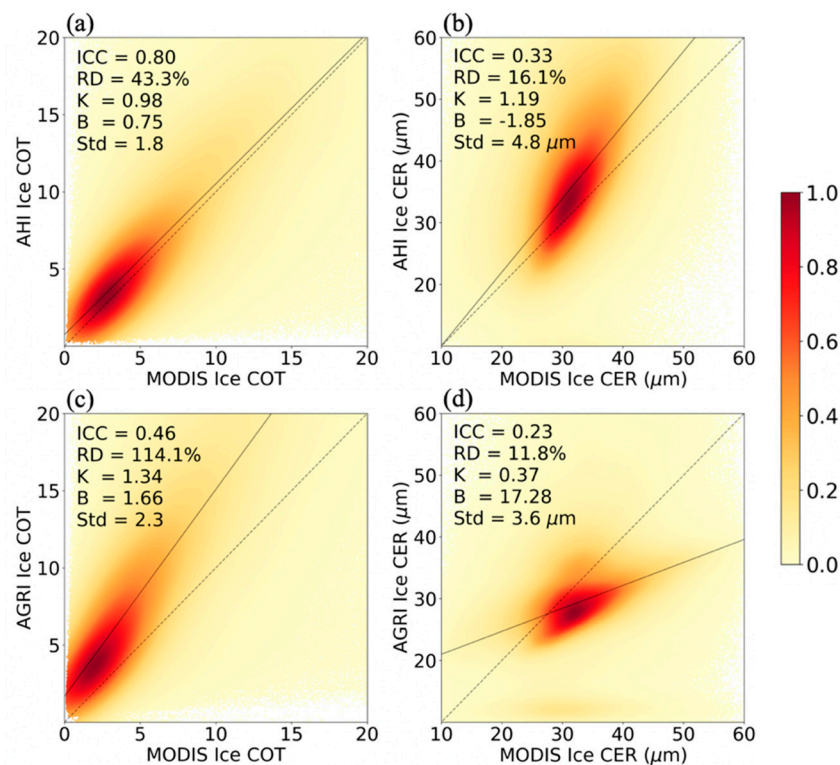


Figure 3. Two-dimensional (2D) histograms of pixel-level comparisons between MODIS and AHI (top row)/AGRI (bottom row) ice cloud properties. The dashed lines are the one-to-one ratio lines. The solid lines are linear regression functions between AHI (AGRI) and MODIS ice cloud properties. The intraclass correlation coefficient (ICC), the average relative difference (RD), the slope (K) and the intercept (B) of the linear regression equation, and the standard deviation (Std) are all plotted in the figure. The color bar indicates the normalized probability density. (a) and (c) COT, and (b) and (d) CER (unit: μm).

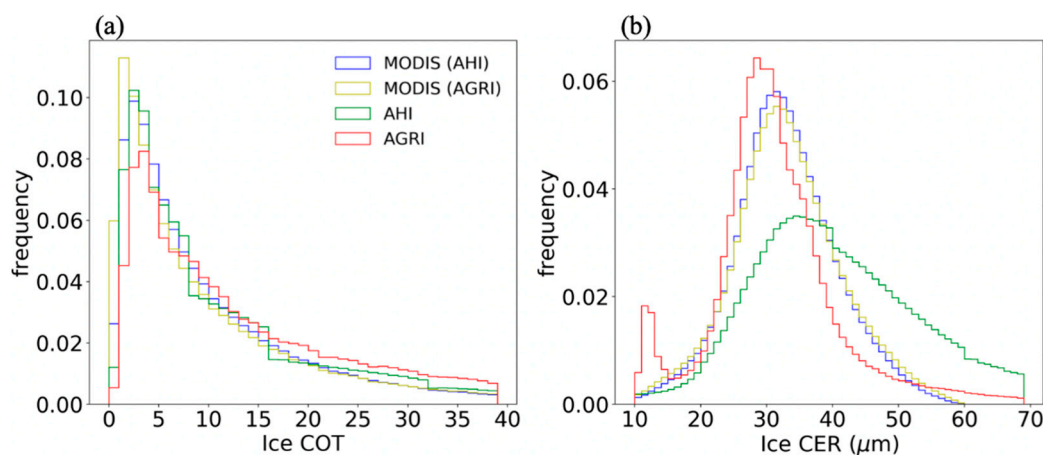


Figure 4. Histograms of the ice cloud property distributions of MODIS, AHI, and AGRI. MODIS (AHI) and MODIS (AGRI) represent the MODIS results of collocation with AHI and AGRI, respectively. (a) COT, (b) CER (unit: μm).

Figure 5 is similar to Figure 3 but for liquid water clouds, and the statistical results are also shown in Table 3. The AHI liquid water COT shows much closer agreement with the MODIS result than that of ice clouds, and the ICC and the slopes are both close to one. With the increase in CER, the results of AHI are smaller than those of MODIS with an ICC and an RD of 0.89 and 8.6%, respectively. Again,

the AGRI products give slightly larger COTs with an RD of 61%. Moreover, the AGRI liquid water CER is systematically overestimated compared with its MODIS counterpart with an RD over 39%.

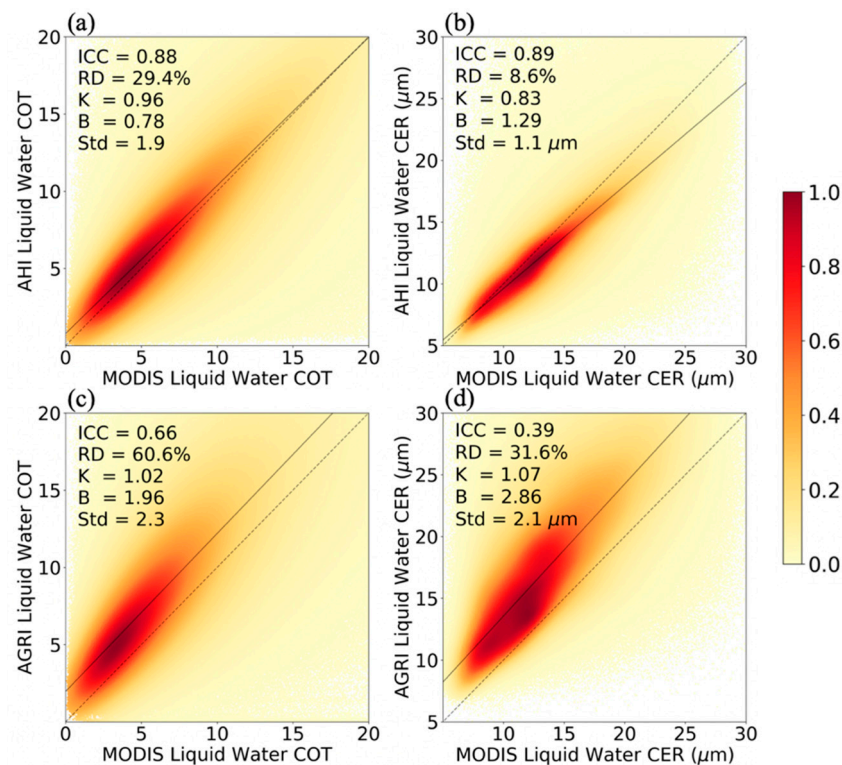


Figure 5. Same as Figure 3 but for liquid water clouds.

The histograms of the occurrence frequencies of liquid water COT and CER are illustrated in Figure 6. The distributions (mainly between 5 and 30 μm) of MODIS and AHI CER are significantly narrower than those of AGRI. As expected, the AHI and the MODIS results have similar distributions. MODIS and AHI show CER peaks of ~ 13 and 10 μm , respectively, which agree with the results shown in Figure 5, and AGRI shows larger frequencies for CERs between ~ 14 and 20 μm .

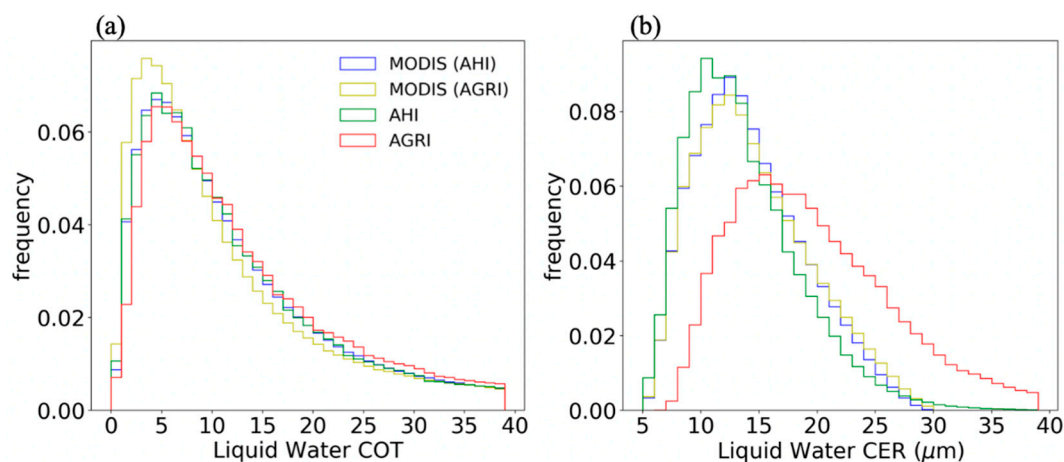


Figure 6. Same as Figure 4 but for liquid water clouds.

Figures 3–6 show that there are clear differences among the AHI, the AGRI, and the MODIS cloud property products, and the magnitudes of the differences are generally similar to those found in other studies. For example, Letu et al. [22] also noticed that AHI ice COTs and CERs are larger than those

of MODIS, but the liquid water results were not studied. Zeng et al. [34] reported that the ice COT of POLDER is substantially smaller than that of MODIS, and the slope is 0.74, corresponding to 0.98 and 1.34 for AHI and AGRI results, respectively. The results of POLDER and MODIS COT show good consistency with a correlation coefficient of 0.92, and those between AHI (AGRI) and MODIS are similar but are not directly reported here.

4. Factors Contributing to the Cloud Property Differences

Multiple factors may contribute to the above differences among AHI, AGRI, and MODIS cloud products, e.g., observation geometry, cloud horizontal inhomogeneity (related to the spatial resolution differences), assumptions for forward radiative transfer models (surface albedo treatment, ice cloud particle models), and retrieval algorithms [31,32,35,62]. Thus, we further discuss the potential factors that could affect the differences in the retrieved COT and CER.

4.1. Differences in the Results Over Land and Ocean

As mentioned in Section 2, AHI, AGRI, and MODIS retrieval algorithms treat the surface similarly but with inevitable differences (even for MODIS and AGRI, which both use the MODIS surface product). Therefore, we first check whether the results over ocean and over land show clear differences.

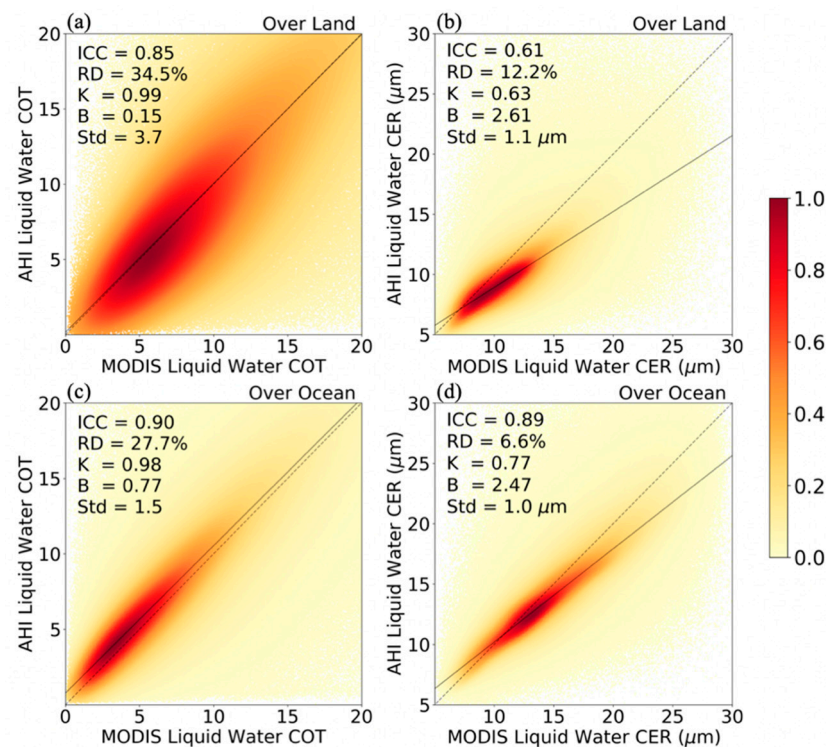


Figure 7. 2D histograms of pixel-level comparisons between MODIS and AHI liquid water cloud properties over land (top row) and ocean (bottom row). The dashed lines are the one-to-one ratio lines. The solid lines are linear regression functions between AHI and MODIS cloud properties. The intraclass correlation coefficient (ICC), the average relative difference (RD), the slope (K) and the intercept (B) of the linear regression equation, and the standard deviation (Std) are all plotted in the figure. The color bar indicates the normalized probability density. (a) and (c) COT, and (b) and (d) CER (unit: μm).

Figure 7 provides pixel-to-pixel comparisons of liquid water clouds over land (top row) and ocean (bottom row) between the AHI and the MODIS products, and Figure 8 is the same but for AGRI and MODIS. The COTs of AHI, AGRI, and MODIS over land are significantly larger than those over ocean, whereas the CERs over land are smaller than those over ocean. Figure 7 indicates that the differences in the cloud properties between AHI and MODIS over land are larger than those over ocean, in particular

for CER, with its ICC increasing from 0.61 to 0.89 and its RD dropping from 12.2% to 6.6%. More clearly, the Std for results over ocean (1.5) is much smaller than the corresponding value over land (3.7) due to the significant variations in the surface albedos over land. In Figure 8, the AGRI liquid water results over land agree more closely with the MODIS results than with those over ocean, especially CER, with an RD from 21.7% over land to 39.7% over ocean. Moreover, the differences in AHI, AGRI, and MODIS ice cloud properties over different surfaces are less significant than those in liquid water clouds; for example, the ICCs of AHI and MODIS ice COTs are 0.77 over land and 0.81 over ocean, respectively. Thus, the ice cloud results are not shown here. Although the treatment of surface albedo is similar in their retrieval algorithms, there are still some differences in optical properties of different instruments over land and ocean.

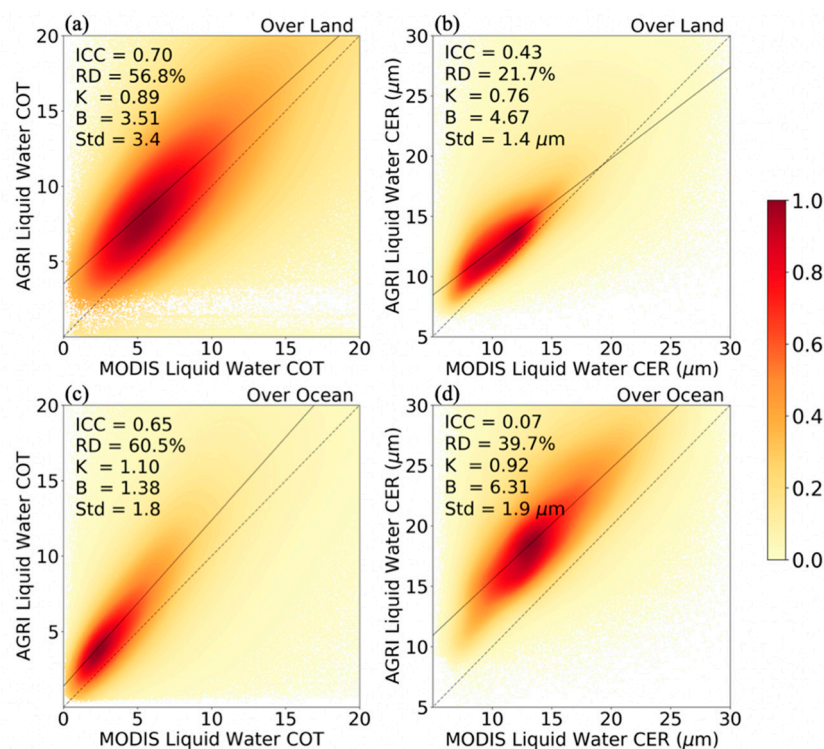


Figure 8. Same as Figure 7 but for the difference between AGRI and MODIS liquid water clouds.

4.2. Impact of the Observation Geometry

The next factor we discuss is the observational geometry. Because of the complex vertical structure of clouds (i.e., their spacing, shape, and orientation), the cloud observation characteristics over the same area observed from different viewing zenith angles (VZA) may differ [63]. To illustrate the effects of this factor on the cloud properties of AHI, AGRI, and MODIS, we discuss the sensitivities of differences with respect to the geometry of satellite observations. For simplicity, we consider only liquid water clouds over ocean, which gives the best agreement between AHI (AGRI) and MODIS. Figure 9 illustrates the distributions of the AHI and the AGRI water cloud COTs (top row) and the corresponding RDs from the MODIS results (bottom row) over ocean within the 80°E–150°E region. We collect all collocated pixels over the region in the studied period, and Figure 9a,b show the average COT over this region. Note that AHI and AGRI are located at 140.7°E and 104.7°E, respectively, and, with departure from the sub-satellite point (marked by the red star in the figure), the viewing zenith angle of geostationary instruments increase. For example, the VZAs of AHI and AGRI for pixels at high latitudes reach over 60°. Thus, possibly due to the increase in the pass length with a larger VZA, the COTs of AHI and AGRI increase. In addition, the changes in average values of COT with VZAs of AHI and AGRI are shown in Table 4. The average COT increases from approximately 7.9 to 12.1 for AHI and from 8.5 to approximately 28.3 for AGRI. Moreover, the COT RDs between the geostationary satellites

instruments and the MODIS increase with AHI (AGRI) VZAs in Figure 9c,d, especially for AGRI. The RDs between AGRI and MODIS increase from approximately 28% to 150% as pixels depart from the sub-satellite point. A possible reason for this result is the plane-parallel assumption made in retrieval algorithms, because the heterogeneity in clouds at vertical spatial scales and the three-dimensional radiation effect are normally not considered in cloud retrievals [6]. Meanwhile, parallax correction is not performed during the collocation, resulting in large differences for pixels with larger viewing zenith angles.

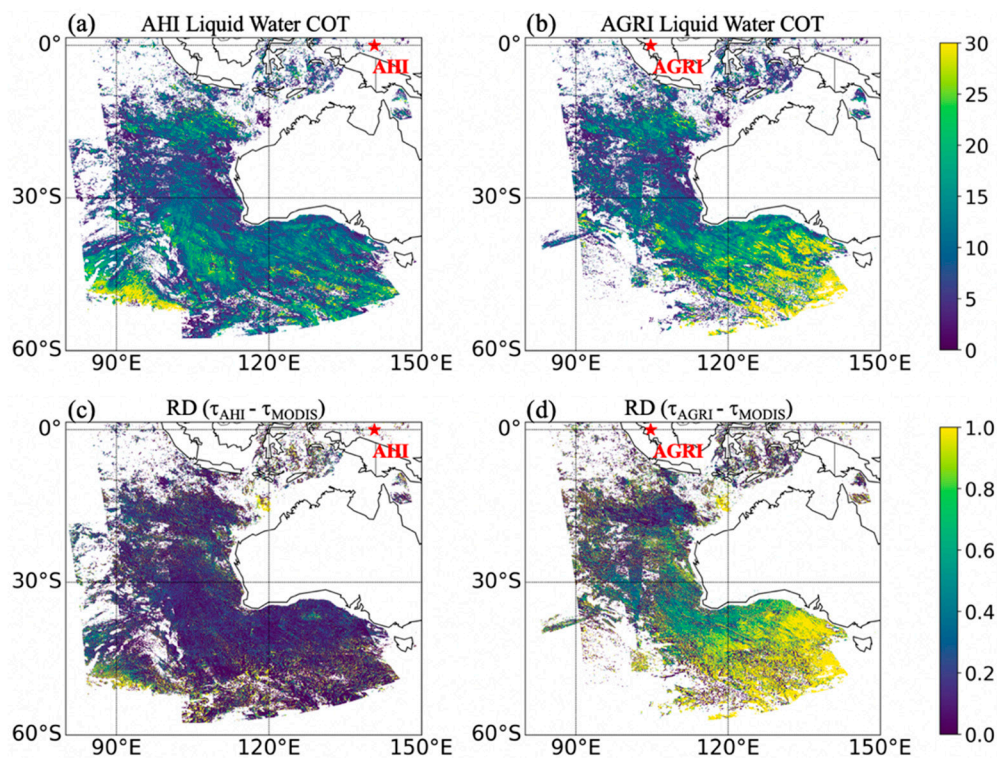


Figure 9. Spatial distributions of the AHI and the AGRI liquid water COTs (**top row**) for over ocean and the RD of liquid water COTs among AHI, AGRI, and MODIS (**bottom row**) for the different viewing zenith angles (VZAs).

Table 4. The average COTs and their RDs at different VZAs of AHI and AGRI.

VZA	0–10°	10–20°	20–30°	30–40°	40–50°	50–60°	60–70°
τ_{AHI}	7.9	9.4	9.1	13.6	11.0	11.2	12.1
τ_{AGRI}	8.5	10.8	8.8	9.2	12.9	20.6	28.3
RD ($\tau_{\text{AHI-MODIS}}$)	38%	37%	28%	27%	19%	18%	21%
RD ($\tau_{\text{AGRI-MODIS}}$)	28%	34%	44%	43%	62%	115%	152%

4.3. Impact of Cloud Inhomogeneity

In the process of retrieving cloud properties, each cloudy pixel is considered to be independent of its neighboring pixels [64]. Therefore, differences among neighboring MODIS pixel (with the original spatial resolution of 1 km) cloud properties may affect cloud properties of the collocated AHI and AGRI pixels (with product spatial resolutions of 4 km and 5 km). In other words, the horizontal homogeneity of cloudy pixels is also a potential contributor to differences in COT and CER, because there are over 10 MODIS pixels within each AHI or AGRI pixel. To describe the homogeneity of geostationary cloudy pixels, we use a ratio (δ) of the standard deviation to the average of MODIS COTs within each AHI (AGRI) pixel. The median T of the ratios δ is used to roughly separate homogeneous

and inhomogeneous clouds. The collocated pixels with $\delta < T$ are referred to as homogeneous clouds, and those with $\delta > T$ are considered as inhomogeneous ones.

Figure 10 illustrates the δ distribution of MODIS COT within AHI pixels (left panels) and pixel-to-pixel comparisons of AHI and MODIS COTs for inhomogeneous (middle panels) and homogeneous clouds (right panels). The δ of ice clouds is mostly less than 0.07, and larger values are shown for water cloud δ . The medians for ice and liquid water clouds are 0.10 and 0.19, respectively. For ice COT, the ICC increases from 0.65 for inhomogeneous clouds to 0.86 for homogeneous ones, and the RD for homogeneous clouds is approximately 17% smaller than the RD of inhomogeneous ones. For liquid water COT, its RD also decreases from 38.0% for inhomogeneous clouds to 22.7% for homogeneous clouds. The AHI CER and AGRI cloud products have similar results to MODIS (not shown). This result shows that cloud horizontal inhomogeneity significantly affects the differences between the cloud products of different instruments, and the agreements can be improved by constraining the homogeneity of the pixels.

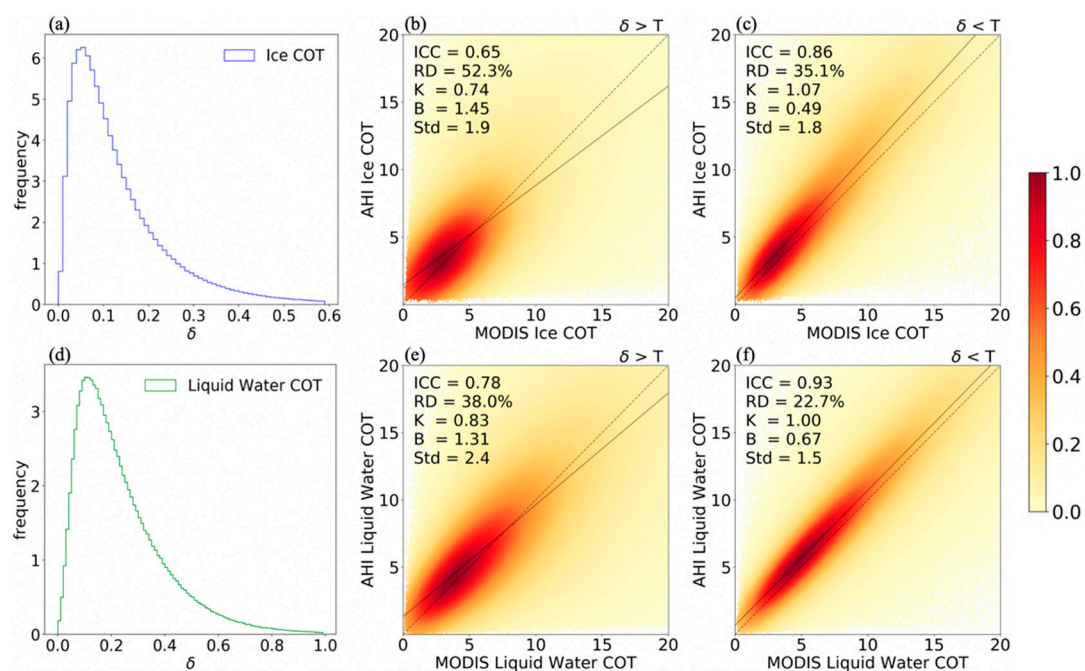


Figure 10. Histograms of the ratio (δ) distributions (left panels) and 2D histograms of pixel-level comparisons between MODIS and AHI liquid water COTs for inhomogeneous (middle panels) and homogeneous (right panels) clouds. The dashed lines are the one-to-one ratio lines. The solid lines are linear regression functions between AHI and MODIS COTs. The intraclass correlation coefficient (ICC), the average relative difference (RD), the slope (K) and the intercept (B) of the linear regression equation, and the standard deviation (Std) are all plotted in the figure. The color bar indicates the normalized probability density.

4.4. Impact of the Retrieval Systems

Although the same Nakajima–King scheme [51] is used for COT and CER retrievals of all three instruments, the retrieval results can be significantly different due to differences in assumed auxiliary parameters, band differences, and forward radiative transfer simulations. For example, only by updating the ice cloud model used for COT and CER retrievals can the MODIS products from different version collections be very different [27,29], because forward radiative transfer models give quite different radiances with different model setups. To investigate the contribution of the cloud property retrieval system itself to the differences among AHI, AGRI, and MODIS cloud products, this study evaluates the retrieval results based on the three instruments measurements using a unified retrieval system.

Here, the “unified retrieval system” refers to using the same retrieval method, forward model, and auxiliary data. First, the retrieval algorithm of the Nakajima–King scheme itself is straightforward and completely the same for different instruments. This study uses the optimal estimation method given by Rodgers [65]. The most significant difference is parameters in the forward model (e.g., same cloud scattering properties, radiative transfer simulation, surface treatment, and atmospheric profiles). Although we use similar bands from these instruments for the Nakajima–King scheme [51]—0.86 and 2.1 μm bands for MODIS, 0.86 and 2.30 μm bands for AHI, and 0.825 and 2.25 μm bands for AGRI—the radiative transfer models (that follow Liu et al. [66]) have to be set up specifically according to spectral response functions (SRFs) of each required band. The model uses a combination of the correlated k-distribution method for the gas transmittances and the LUT-based method for cloud multiple scattering [66,67], and the differences in the SRFs are considered for both methods. The ice optical properties of the severely roughened hexagonal aggregates of the MODIS C6 products are used [68], and the optical properties of water droplets are from those of Mie calculations. To avoid the influence of strong surface reflectance, we consider pixels over ocean, and the surface albedos at cloud non-absorbing and absorbing bands are kept the same for all three instruments. MODIS, AHI, and AGRI show noticeable differences in the cloud absorbing bands with central wavelengths at 2.13, 2.30, and 2.25 μm , resulting in different cloud absorptions. These differences can be used for cloud phase and multilayer cloud detections [69–71]. This study ensures only that SRF differences are accounted for in the forward simulations, whereas the potential influences on the retrieved CERs due to the different cloud absorptions and cloud vertical inhomogeneity is not discussed [36].

Similar to Figures 3 and 5, Figures 11 and 12 show pixel-to-pixel comparisons of COTs and CERs, respectively, among the three instruments but using the unified retrieval system. The corresponding statistical analysis results are given in figures and Table 5. Figure 11 is for ice cloud properties. The COT and the CER values using the unified retrieval system to retrieve for AHI and AGRI are smaller than their products, except for AGRI CER, and the correlation between them is also significantly changed. Evidently, this change can be seen from the ICC, the RD, and the slope of cloud properties for different instruments. For example, the COT RD of AHI and MODIS can be optimized by approximately 37% compared to that of their own products, and, for AHI CER, the RD is also reduced by approximately 50%. This result shows that, for optical properties of AHI and MODIS ice clouds, using the unified retrieval system can improve the consistency. In the comparison between AGRI and MODIS COT, it is noted that the retrieval results have a good correlation with an ICC increasing from 0.46 to 0.84, and the RD is reduced by ~77% compared with the results of their products. The slope between AGRI and MODIS ice CER increases from 0.37 for their products to 0.98 for the retrieval results, and their ICC values also increase from 0.2 to 0.6. From the perspective of liquid water clouds shown in Figure 12, the retrieval results of AHI do not change much compared to its operational products. However, the AGRI retrieval optical properties (i.e., COT and CER) are smaller than its products. It is observed that the RD of COT decreases from 60.6% to 27.1%, and their ICC values increase from 0.66 to 0.84. The RD of CER is also optimized to its product by approximately 69%. This result means that the change in retrieval system has an important impact on the retrieved optical properties of clouds. By using the unified retrieval algorithm to retrieve cloud properties with different instruments, it is found that their consistency is significantly improved, especially for ice clouds. This result indicates that the differences in cloud optical properties from MODIS, AHI, and AGRI are largely due to the differences in the retrieval spectral and the forward models.

Through the discussion in this section, the differences between the AHI (AGRI) and the MODIS cloud properties are shown to be related to the observational geometry, the cloud horizontal inhomogeneity, and, most importantly, the retrieval systems of these instruments, which can cause 30% to 70% of those differences. The rest of the differences may be contributed by calibration errors, parallax errors, different sensitivities of different cloud absorbing bands (among the 2.13, the 2.25, and the 2.30 μm bands), etc. The influences of those potential factors will be investigated in further studies.

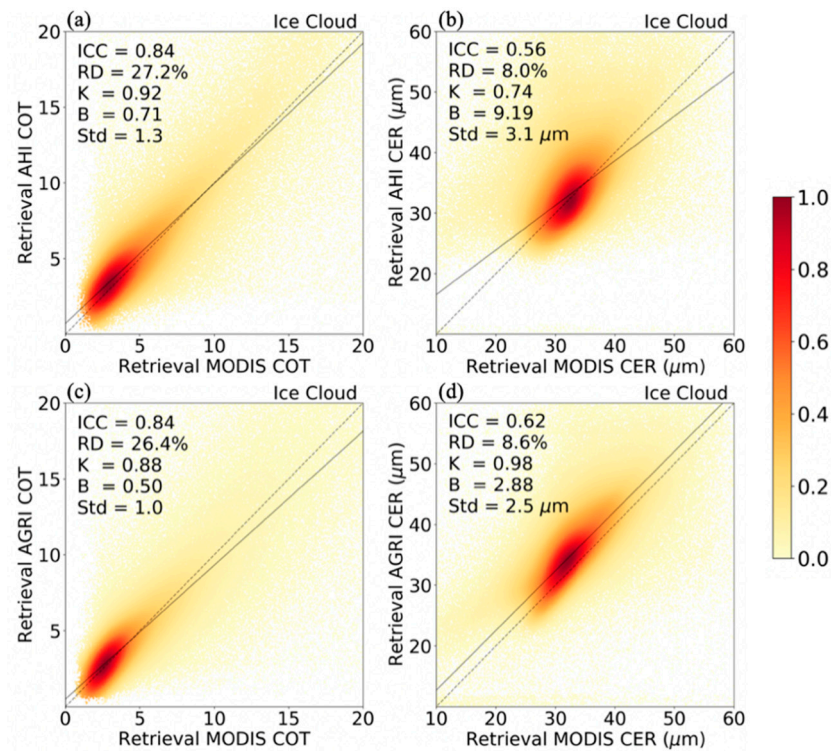


Figure 11. Same as Figure 3 but for ice cloud properties retrieved from our unified retrieval system.

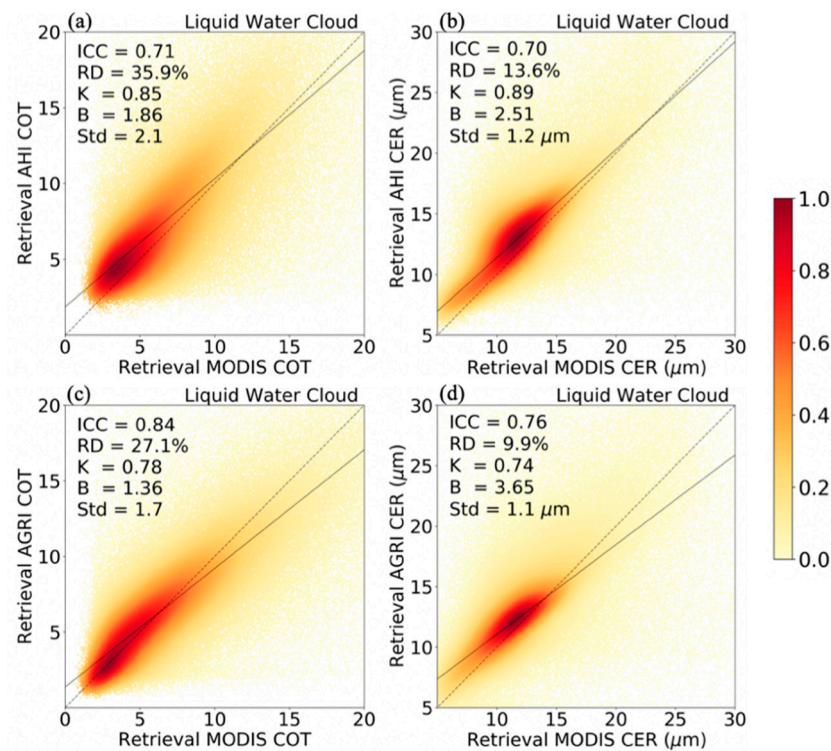


Figure 12. Same as Figure 11 but for liquid water clouds.

Table 5. Similar to Table 3 but for the retrieval of cloud properties by using a unified retrieval system.

		AHI					AGRI				
		K	B	ICC	RD	Std	K	B	ICC	RD	Std
Ice	COT	0.92	0.71	0.84	27.2%	1.3	0.88	0.50	0.84	26.4%	1.0
	CER	0.74	9.19	0.56	8.0%	3.1	0.98	2.88	0.62	8.6%	2.5
Water	COT	0.85	1.86	0.71	35.9%	2.1	0.78	1.36	0.84	27.1%	1.7
	CER	0.89	2.51	0.70	13.6%	1.2	0.74	3.65	0.76	9.9%	1.1

5. Conclusions

This study compares cloud mask, phase, and microphysics and optical properties (i.e., COT and CER) of MODIS, AHI, and AGRI level-2 cloud products to better understand the cloud observation characteristics of the two Asian geostationary satellites (i.e., AHI/H-8 and AGRI/FY-4A). AHI, AGRI, and MODIS give similar cloud classifications, and both the cloud mask and the phase of AHI and AGRI have HRs of over 70% compared with MODIS results. The most significant differences in cloud mask are observed in the pro-clear or pro-cloudy pixels, and the differences in cloud phase are from mixed-phase clouds. To be more specific, AHI gives more pro-cloudy pixels, and AGRI gives fewer pro-cloudy pixels. AHI (AGRI) may identify certain water or ice clouds as mixed-phase clouds. The AHI ice COTs are systematically larger than those of MODIS with an RD of ~43%, and this difference becomes more notable as COT increases. The AGRI ice COT shows even larger differences than the corresponding MODIS COT. The AHI ice CER is larger than that of AGRI and MODIS, and it is distributed over a wider range. The AGRI ice CER shows bimodal peaks at approximately 12 and 28 μm , and it is slightly smaller than that of MODIS. The liquid water COT and CER of AHI agree with those of MODIS most closely with an RD below 30%, whereas the AGRI liquid water results still show notable RDs from those of MODIS.

To better understand these differences, we discuss the potential factors (i.e., surface albedo treatment, observation geometry, cloud horizontal inhomogeneity, and retrieval system) that may cause them. The differences in the RDs over land and ocean indicate that different treatments of the surface albedos in different retrievals result in certain differences. The differences between ice and liquid water cloud optical properties of AHI and MODIS over land are greater than those over ocean, whereas the AGRI and the MODIS results agree more closely over land. The AGRI liquid water COT and its RD between AGRI and MODIS increase with viewing zenith angle, which is caused by the heterogeneity and the three-dimensional radiation effects of clouds. The RDs of COTs from different instruments for homogeneous clouds are ~30% smaller than corresponding RDs for inhomogeneous clouds. By introducing the “completely” unified retrieval system, the RDs between AHI and MODIS for ice cloud COT and CER decrease by 37% and 50%, respectively, compared with the RDs from the direct comparisons of their operational products. The results of AHI and MODIS liquid water properties are not significantly changed. Moreover, the consistencies of AGRI clouds properties with those of MODIS are significantly improved, and their RDs all are optimized by more than 50%. To summarize, although AHI and AGRI can provide high spatial and temporal resolution observations for clouds in Asia, their results should be examined more closely in future studies.

Author Contributions: Conceptualization, R.L., C.L. and S.T.; data curation, R.L.; methodology, R.L. and S.T.; resources, H.L., M.M. and S.T.; validation, R.L. and C.L.; writing—original draft preparation, R.L.; C.L. and B.Y.; writing—review and editing, S.T., B.Y., H.L., M.M., S.T. and C.L.

Funding: This research was funded by National Key Research and Development Program of China (2018YFC1506502), the National Natural Science Foundation of China (41571348, 41775130), and Young Elite Scientists Sponsorship Program by CAST (2017QNRC001).

Conflicts of Interest: The authors declare no conflict of interest.

References

- Baker, M.B.; Peter, T. Small-scale cloud processes and climate. *Nature* **2008**, *451*, 299–300. [[CrossRef](#)] [[PubMed](#)]
- Liou, K.N. Influence of cirrus clouds on weather and climate processes: A global perspective. *Mon. Weather Rev.* **1986**, *114*, 1167–1199. [[CrossRef](#)]
- Stephens, G.L.; Tsay, S.C.; Stackhouse, P.W.; Flatau, P.J. The relevance of the microphysical and radiative properties of cirrus clouds to climate and climate feedback. *J. Atmos. Sci.* **1990**, *47*, 1742–1753. [[CrossRef](#)]
- Kinne, S.; Liou, K.N. The effects of the nonsphericity and size distribution of ice crystals on the radiative properties of cirrus clouds. *Atmos. Res.* **1989**, *24*, 273–284. [[CrossRef](#)]
- Heymsfield, A.J. Properties of tropical and midlatitude ice cloud particle ensembles. Part I: Median mass diameters and terminal velocities. *J. Atmos. Sci.* **2003**, *60*, 2573–2591. [[CrossRef](#)]
- Zinner, T.; Mayer, B. Remote sensing of stratocumulus clouds: Uncertainties and biases due to inhomogeneity. *J. Geophys. Res.* **2006**, *111*. [[CrossRef](#)]
- Schnaiter, M.; Järvinen, E.; Vochezer, P.; Abdelmonem, A.; Wagner, R.; Jourdan, O.; Ulanowski, Z. Cloud chamber experiments on the origin of ice crystal complexity in cirrus clouds. *Atmos. Chem. Phys.* **2016**, *16*, 5091–5110. [[CrossRef](#)]
- Lawson, R.P.; Baker, B.; Pilon, B.; Mo, Q. In situ observations of the microphysical properties of wave, cirrus, and anvil clouds. Part II: Cirrus clouds. *J. Atmos. Sci.* **2006**, *63*, 3186–3203. [[CrossRef](#)]
- Vivekanandan, J.; Zrnich, D.S.; Ellis, S.M.; Oye, R.; Ryzhkov, A.V.; Straka, J. Cloud microphysics retrieval using S-band dual-polarization radar measurements. *Bull. Am. Meteorol. Soc.* **1999**, *80*, 381–388. [[CrossRef](#)]
- Stephens, G.L.; Vane, D.G.; Boain, R.J.; Mace, G.G.; Sassen, K.; Wang, Z.; Illingworth, A.J.; O’connor, E.J.; Rossow, W.B.; Durden, S.L.; et al. The CloudSat mission and the A-Train: A new dimension of space-based observations of clouds and precipitation. *Bull. Am. Meteorol. Soc.* **2002**, *83*, 1771–1790. [[CrossRef](#)]
- Kidd, C.; Levizzani, V.; Bauer, P. A review of satellite meteorology and climatology at the start of the twenty-first century. *Prog. Phys. Geogr.* **2009**, *33*, 474–489. [[CrossRef](#)]
- King, M.D.; Platnick, S.; Menzel, W.P.; Ackerman, S.A.; Hubanks, P.A. Spatial and temporal distribution of clouds observed by MODIS onboard the Terra and Aqua satellites. *IEEE Trans. Geosci. Remote Sens.* **2013**, *51*, 3826–3852. [[CrossRef](#)]
- King, M.D.; Menzel, W.P.; Kaufman, Y.J.; Tanré, D.; Gao, B.C.; Platnick, S.; Ackerman, S.A.; Remer, L.A.; Pincus, R.; Hubanks, P.A. Cloud and aerosol properties, precipitable water, and profiles of temperature and water vapor from MODIS. *IEEE Trans. Geosci. Remote Sens.* **2003**, *41*, 442–458. [[CrossRef](#)]
- Dong, C.; Yang, J.; Zhang, W.; Yang, Z.; Lu, N.; Shi, J.; Zhang, P.; Liu, Y.; Cai, B. An overview of a new Chinese weather satellite FY-3A. *Bull. Am. Meteorol. Soc.* **2009**, *90*, 1531–1544. [[CrossRef](#)]
- Zhang, P.; Yang, J.; Dong, C.; Lu, N.; Yang, Z.; Shi, J. General introduction on payloads, ground segment and data application of Fengyun 3A. *Front. Earth Sci. China* **2009**, *3*, 367–373. [[CrossRef](#)]
- Im, E.; Wu, C.; Durden, S.L. Cloud profiling radar for the CloudSat mission. In Proceedings of the IEEE International Radar Conference, Arlington, VA, USA, 9–12 May 2005.
- Winker, D.M.; Pelon, J.R.; McCormick, M.P. The CALIPSO mission: Spaceborne lidar for observation of aerosols and clouds. *Proc. SPIE Int. Soc. Opt. Eng.* **2003**, *4893*, 1–11.
- Schmit, T.J.; Gunshor, M.M.; Menzel, W.P.; Gurka, J.J.; Li, J.; Bachmeier, A.S. Introducing the next-generation Advanced Baseline Imager on GOES-R. *Bull. Am. Meteorol. Soc.* **2005**, *86*, 1079–1096. [[CrossRef](#)]
- Da, C. Preliminary assessment of the Advanced Himawari Imager (AHI) measurement onboard Himawari-8 geostationary satellite. *Remote Sens. Lett.* **2015**, *6*, 637–646. [[CrossRef](#)]
- Yang, J.; Zhang, Z.; Wei, C.; Lu, F.; Guo, Q. Introducing the new generation of Chinese geostationary weather satellites—FengYun 4 (FY-4). *Bull. Am. Meteorol. Soc.* **2017**, *98*, 1637–1658. [[CrossRef](#)]
- Bessho, K.; Date, K.; Hayashi, M.; Ikeda, A.; Imai, T.; Inoue, H.; Kumagai, Y.; Miyakawa, T.; Murata, H.; Ohno, T.; et al. An introduction to Himawari-8/9-Japan’s new-generation geostationary meteorological satellites. *J. Meteorol. Soc. Jpn.* **2016**, *94*, 151–183. [[CrossRef](#)]
- Letu, H.; Nagao, T.M.; Nakajima, T.Y.; Riedi, J.; Ishimoto, H.; Baran, A.J.; Shang, H.; Sekiguchi, M.; Kikuchi, M. Ice cloud properties from Himawari-8/AHI next-generation geostationary satellite: Capability of the AHI to monitor the DC cloud generation process. *IEEE Trans. Geosci. Remote Sens.* **2018**, *56*, 3229–3239. [[CrossRef](#)]
- Lu, F.; Shou, Y. Channel simulation for FY-4 AGRI. In Proceedings of the 2011 IEEE International Geoscience and Remote Sensing Symposium, Vancouver, CU, Canada, 24–29 July 2011; pp. 3265–3268.

24. Chen, D.; Guo, J.; Wang, H.; Li, J.; Min, M.; Zhao, W.; Yao, D. The cloud top distribution and diurnal variation of clouds over East Asia: Preliminary results from Advanced Himawari Imager. *J. Geophys. Res.* **2018**, *123*, 3724–3739. [[CrossRef](#)]
25. Shang, H.; Letu, H.; Nakajima, T.Y.; Wang, Z.; Ma, R.; Wang, T.; Lei, Y.; Ji, D.; Li, S.; Shi, J. Diurnal cycle and seasonal variation of cloud cover over the Tibetan Plateau as determined from Himawari-8 new-generation geostationary satellite data. *Sci. Rep.* **2018**, *8*, 1–8. [[CrossRef](#)] [[PubMed](#)]
26. Hong, G.; Yang, P.; Gao, B.C.; Baum, B.A.; Hu, Y.X.; King, M.D.; Platnick, S. High cloud properties from three years of MODIS Terra and Aqua collection-4 Data over the tropics. *J. Appl. Meteorol. Clim.* **2007**, *46*, 1840–1856. [[CrossRef](#)]
27. Yang, P.; Zhang, L.; Hong, G.; Nasiri, S.L.; Baum, B.A.; Huang, H.L.; King, M.D.; Platnick, S. Differences between collection 4 and 5 MODIS ice cloud optical/microphysical products and their impact on radiative forcing simulations. *IEEE Trans. Geosci. Remote Sens.* **2007**, *45*, 2886–2899. [[CrossRef](#)]
28. Platnick, S.; Meyer, K.G.; King, M.D.; Wind, G.; Amarasinghe, N.; Marchant, B.; Arnold, G.T.; Zhang, Z.; Hubanks, P.A.; Holz, R.E.; et al. The MODIS cloud optical and microphysical products: Collection 6 updates and examples from Terra and Aqua. *IEEE Trans. Geosci. Remote Sens.* **2017**, *55*, 502–525. [[CrossRef](#)]
29. Yi, B.; Rapp, A.D.; Yang, P.; Baum, B.A.; King, M.D. A comparison of Aqua MODIS ice and liquid water cloud physical and optical properties between collection 6 and collection 5.1: Pixel-to-pixel comparisons. *J. Geophys. Res.* **2017**, *122*, 4528–4549. [[CrossRef](#)]
30. Yi, B.; Rapp, A.D.; Yang, P.; Baum, B.A.; King, M.D. A comparison of Aqua MODIS ice and liquid water cloud physical and optical properties between collection 6 and collection 5.1: Cloud radiative effects. *J. Geophys. Res.* **2017**, *122*, 4550–4564. [[CrossRef](#)]
31. Yi, B.; Yang, P.; Baum, B.A.; L'Ecuyer, T.; Oreopoulos, L.; Mlawer, E.J.; Heymsfield, A.J.; Liou, K.-N. Influence of ice particle surface roughening on the global cloud radiative effect. *J. Atmos. Sci.* **2013**, *70*, 2794–2807. [[CrossRef](#)]
32. Zhang, Z.; Yang, P.; Kattawar, G.; Riedi, J.; Labonnote, L.C.; Baum, B.A.; Platnick, S.; Huang, H.L. Influence of ice particle model on satellite ice cloud retrieval: Lessons learned from MODIS and POLDER cloud product comparison. *Atmos. Chem. Phys.* **2009**, *9*, 7115–7129. [[CrossRef](#)]
33. Zhang, Z.; Yang, P.; Kattawar, G.W.; Tsay, S.-C.; Baum, B.A.; Hu, Y.; Heymsfield, A.J.; Reichardt, J. Geometrical-optics solution to light scattering by droxtal ice crystals. *Appl. Opt.* **2004**, *43*, 2490–2499. [[CrossRef](#)]
34. Zeng, S.; Cornet, C.; Parol, F.; Riedi, J.; Thieuleux, F. A better understanding of cloud optical thickness derived from the passive sensors MODIS/AQUA and POLDER/PARASOL in the A-Train constellation. *Atmos. Chem. Phys.* **2012**, *12*, 11245–11259. [[CrossRef](#)]
35. Kahn, B.H.; Schreier, M.M.; Yue, Q.; Fetzer, E.J.; Irion, F.W.; Platnick, S.; Wang, C.; Nasiri, S.L.; L'Ecuyer, T.S. Pixel-scale assessment and uncertainty analysis of AIRS and MODIS ice cloud optical thickness and effective radius. *J. Geophys. Res.* **2015**, *120*, 11669–11689. [[CrossRef](#)]
36. Zhang, Z.; Platnick, S.; Yang, P.; Heidinger, A.K.; Comstock, J.M. Effects of ice particle size vertical inhomogeneity on the passive remote sensing of ice clouds. *J. Geophys. Res.* **2010**, *115*. [[CrossRef](#)]
37. Wang, C.; Platnick, S.; Fauchez, T.; Meyer, K.; Zhang, Z.; Iwabuchi, H.; Kahn, B.H. An assessment of the impacts of cloud vertical heterogeneity on global ice cloud data records from passive satellite retrievals. *J. Geophys. Res.* **2019**, *124*, 1578–1595. [[CrossRef](#)]
38. Min, M.; Wu, C.; Li, C.; Xu, N.; Wu, X.; Chen, L.; Wang, F.; Sun, F.; Qin, D.; Wang, X.; et al. Developing the science product algorithm testbed for Chinese next-generation geostationary meteorological satellites: Fengyun-4 series. *J. Meteorol. Res.* **2017**, *31*, 708–719. [[CrossRef](#)]
39. King, M.D.; Kaufman, Y.J.; Menzel, W.P.; Tanre, D. Remote sensing of cloud, aerosol, and water vapor properties from the Moderate Resolution Imaging Spectrometer (MODIS). *IEEE Trans. Geosci. Remote Sens.* **1992**, *30*, 2–27. [[CrossRef](#)]
40. Ham, S.H.; Sohn, B.J.; Yang, P.; Baum, B.A. Assessment of the quality of MODIS cloud products from radiance simulations. *J. Appl. Meteorol. Clim.* **2009**, *48*, 1591–1612. [[CrossRef](#)]
41. Xiong, X.; Wenny, B.N.; Wu, A.; Barnes, W.L.; Salomonson, V.V. Aqua MODIS thermal emissive band on-orbit calibration, characterization, and performance. *IEEE Trans. Geosci. Remote Sens.* **2009**, *47*, 803–814. [[CrossRef](#)]

42. Gao, B.C.; Yang, P.; Guo, G.; Park, S.K.; Wiscombe, W.J.; Chen, B. Measurements of water vapor and high clouds over the Tibetan Plateau with the Terra MODIS instrument. *IEEE Trans. Geosci. Remote Sens.* **2003**, *41*, 895–900.
43. Meyer, K.; Yang, P.; Gao, B.C. Tropical ice cloud optical depth, ice water path, and frequency fields inferred from the MODIS level-3 data. *Atmos. Res.* **2007**, *85*, 171–182. [[CrossRef](#)]
44. Oreopoulos, L.N.; Cho, N.; Lee, D.; Kato, S.; Huffman, G.J. An examination of the nature of global MODIS cloud regimes. *J. Geophys. Res.* **2014**, *119*, 8362–8383. [[CrossRef](#)]
45. Ackerman, S.A.; Strabala, K.I.; Menzel, W.P.; Frey, R.A.; Moeller, C.C.; Gumley, L.E. Discriminating clear sky from clouds with MODIS. *J. Geophys. Res.* **1998**, *103*, 32141–32157. [[CrossRef](#)]
46. Imai, T.; Yoshida, R. Algorithm theoretical basis for Himawari-8 cloud mask product. *Meteorol. Satell. Cent. Tech.* **2017**, *61*, 1–17.
47. Wang, X.; Min, M.; Wang, F.; Guo, J.; Li, B.; Tang, S. Inter-comparisons of cloud mask product among Fengyun-4A, Himawari-8 and MODIS. *IEEE Trans. Geosci. Remote Sens.* **2019**. [[CrossRef](#)]
48. Marchant, B.; Platnick, S.; Meyer, K.; Arnold, G.T.; Riedi, J. MODIS collection 6 shortwave-derived cloud phase classification algorithm and comparisons with CALIOP. *Atmos. Meas. Tech.* **2016**, *9*, 1587–1599. [[CrossRef](#)]
49. Mouri, K.; Izumi, T.; Suzue, H.; Yoshida, R. Algorithm Theoretical Basis Document of cloud type/phase product. *Meteorol. Satell. Cent. Tech.* **2016**, *61*, 19–31.
50. Pavolonis, M.J.; Heidinger, A.K.; Uttal, T. Daytime global cloud typing from AVHRR and VIIRS: Algorithm description, validation, and comparisons. *J. Appl. Meteorol.* **2006**, *44*, 804–826. [[CrossRef](#)]
51. Nakajima, T.; King, M.D. Determination of the optical thickness and effective particle radius of clouds from reflected solar radiation measurements. Part I: Theory. *J. Atmos. Sci.* **1990**, *47*, 1878–1893. [[CrossRef](#)]
52. King, M.D.; Tsay, S.C.; Platnick, S.E.; Wang, M.; Liou, K.N. *Cloud Retrieval Algorithms for MODIS: Optical Thickness, Effective Particle Radius, and Thermodynamic Phase*; NASA Goddard Space Flight Center: Greenbelt, MD, USA, 1997.
53. Nakajima, T.Y.; Nakajima, T. Wide-area determination of cloud microphysical properties from NOAA AVHRR measurements for FIRE and ASTEX regions. *J. Atmos. Sci.* **1995**, *52*, 4043–4059. [[CrossRef](#)]
54. Kawamoto, K.; Nakajima, T.; Nakajima, T.Y. A global determination of cloud microphysics with AVHRR remote sensing. *J. Clim.* **2001**, *14*, 2054–2068. [[CrossRef](#)]
55. Walther, A.; Straka, W.; Heidinger, A.K. *ABI Algorithm Theoretical Basis Document for Daytime Cloud Optical and Microphysical Properties (DCOMP)*; NOAA/NESDIS Center Satellite Applications and Research: Camp Springs, MD, USA, 2011; Volume 61. Available online: https://www.goesr.gov/products/ATBDs/baseline/Cloud_DCOMP_v2.0_no_color.pdf (accessed on 1 July 2019).
56. Yang, P.; Bi, L.; Baum, B.A.; Liou, K.N.; Kattawar, G.W.; Mishchenko, M.I.; Cole, B. Spectrally consistent scattering, absorption, and polarization properties of atmospheric ice crystals at wavelengths from 0.2 to 100 μm . *J. Atmos. Sci.* **2013**, *70*, 330–347. [[CrossRef](#)]
57. Letu, H.; Ishimoto, H.; Nakajima, T.Y.; Baran, A.J.; C-Labonnote, L.; Nagao, T.M.; Sekiguchi, M. Investigation of ice particle habits to be used for ice cloud remote sensing for the GCOM-C satellite mission. *Atmos. Chem. Phys.* **2016**, *16*, 12287–12303. [[CrossRef](#)]
58. Baum, B.A.; Yang, P.; Heymsfield, A.J.; Platnick, S.; King, M.D.; Bedka, S.T. Bulk scattering models for the remote sensing of ice clouds. Part 2: Narrowband models. *J. Appl. Meteorol.* **2005**, *44*, 1896–1911. [[CrossRef](#)]
59. Li, J.; Menzel, W.P.; Sun, F.; Schmit, T.J.; Gurka, J. AIRS subpixel cloud characterization using MODIS cloud products. *J. Appl. Meteorol.* **2004**, *43*, 1083–1094. [[CrossRef](#)]
60. Meteorological Satellite Center (MSC) of JMA. Available online: https://www.data.jma.go.jp/mscweb/data/monitoring/gsics/vis/monit_visvical.html (accessed on 1 July 2019).
61. Sun, L.; Hu, X.; Guo, M.; Xu, N. Multisite calibration tracking for FY-3A MERSI solar bands. *IEEE Trans. Geosci. Remote Sens.* **2012**, *50*, 4929–4942. [[CrossRef](#)]
62. Wu, D.L.; Baum, B.A.; Choi, Y.S.; Foster, M.J.; Karlsson, K.K.; Heidinger, A.; Poulsen, C.; Pavolonis, M.; Riedi, J.; Roebeling, R.; et al. Toward global harmonization of derived cloud products. *Bull. Am. Meteorol. Soc.* **2017**, *9*, ES49–ES52. [[CrossRef](#)]
63. Minnis, P. Viewing zenith angle dependence of cloudiness determined from coincident GOES East and GOES West data. *J. Geophys. Res.* **1989**, *94*, 2303–2320. [[CrossRef](#)]

64. Fauchez, T.; Platnick, S.; Sourdeval, O.; Wang, C.; Meyer, K.; Cornet, C.; Szczap, F. Cirrus horizontal heterogeneity and 3-D radiative effects on cloud optical property retrievals from MODIS near to thermal infrared channels as a function of spatial resolution. *J. Geophys. Res.* **2018**, *123*, 11141–11153. [[CrossRef](#)]
65. Rodgers, C.D. *Inverse Methods for Atmospheric Sounding: Theory and Practice*; World Scientific: Singapore, 2000.
66. Liu, C.; Yang, P.; Nasiri, S.L.; Platnick, S.; Meyer, K.G.; Wang, C.; Ding, S. A fast Visible Infrared Imaging Radiometer Suite simulator for cloudy atmospheres. *J. Geophys. Res.* **2015**, *120*, 240–255. [[CrossRef](#)]
67. Wang, C.; Yang, P.; Baum, B.A.; Platnick, S.; Heidinger, A.K.; Hu, Y.; Holz, R.E. Retrieval of ice cloud optical thickness and effective particle size using a fast radiative transfer model. *J. Appl. Meteorol. Clim.* **2011**, *50*, 2283–2297. [[CrossRef](#)]
68. Zhang, Z.; Yang, P.; Kattawar, G.; Huang, H.L.; Greenwald, T.; Li, J.; Baum, B.A.; Zhou, D.K.; Hu, Y.X. A fast infrared radiative transfer model based on the adding-doubling method for hyperspectral remote-sensing applications. *J. Quant. Spectrosc. Radiat. Transf.* **2007**, *105*, 243–263. [[CrossRef](#)]
69. Kerdraon, G.; Gléau, H.L.; Raoul, M.-P. Combined use of 1.6 and 2.25 micrometer reflectances to improve the cloud phase retrieval in the NWCSAF/GEO cloud microphysics. In Proceedings of the 2015 EUMETSAT Meteorological Satellite Conference, Toulouse, France, 21–25 September 2015.
70. Wang, J.; Liu, C.; Min, M.; Hu, X.; Lu, Q.; Husi, L. Effects and applications of satellite radiometer 2.25- μm channel on cloud property retrievals. *IEEE Trans. Geosci. Remote Sens.* **2018**, *56*, 5207–5216. [[CrossRef](#)]
71. Wang, J.; Liu, C.; Yao, B.; Min, M.; Letu, H.; Yin, Y.; Yung, Y.L. A multilayer cloud detection algorithm for the Suomi-NPP Visible Infrared Imager Radiometer Suite (VIIRS). *Remote Sens. Environ.* **2019**, *227*, 1–11. [[CrossRef](#)]



© 2019 by the authors. Licensee MDPI, Basel, Switzerland. This article is an open access article distributed under the terms and conditions of the Creative Commons Attribution (CC BY) license (<http://creativecommons.org/licenses/by/4.0/>).